Experimental seismic behavior of innovative composite shear walls

Xiaomeng Zhang, Ying Qin, Zhihua Chen *

State Key Laboratory of Hydraulic Engineering Simulation and Safety, Tianjin University, China
Department of Civil Engineering, Tianjin University, Tianjin, China

ABSTRACT

In this paper, an innovative structural wall, named bundled lipped channel–concrete (BLC–C) composite wall, is proposed. The proposed wall consists of bundled lipped channels seam-welded together and in-filled concrete. Seven full-scaled specimens were tested under axial load subjected to cyclic lateral load. The variables studied in the experiments include the configuration of the walls, the axial load ratio, the presence of shear studs, and the loading history. The specimens exhibited ductility and experienced stable hysteresis behavior. The specimens failed in the sequence of local buckling of the steel sheet, and the propagation of the fractures at the boundary of the wall. The seismic behavior of the specimens was evaluated in terms of strength, stiffness, deformation, ductility, and energy dissipation capacity. The results indicate that the level of axial force ratio and the configuration detail significantly affect the entire hysteresis performance, while the presence of shear studs delays the occurrence of fracture and failure.

© 2015 Elsevier Ltd. All rights reserved.

1. Introduction

Traditionally the use of reinforced concrete shear walls has been common in multi-story building to resist lateral load imposed by earthquake or wind [1]. The ductility and the deformation capacity of shear walls are largely affected by the axial load ratio and the wall configuration. Modern codes and standards [2–5] specify the upper limit for the axial load ratio and the lower limit for the requirements on the transverse reinforcement at the confined boundary elements of the walls and thus, resulting in rather thick sections and dense stirrup at the wall boundaries, particularly in lower stories of high-rise buildings, which induces difficulties in construction. In addition, a reinforced concrete shear wall suffers from tension cracks developing in the tension areas while there is compressive crushing occurring in the localized compression zones at large cyclic excursions. Such cracks and crushing lead to splitting and spalling failure of the wall as the cyclic displacements become larger and repeated, which in turn results in severe degradation of strength and reduction in stiffness [6].

Recently, steel plate shear walls [7–8] are becoming increasingly popular for a lateral-load resisting system attributed to many structural and economical merits. On the other hand, the main disadvantage of a steel shear wall lies in the development of local buckling in the compression areas, which leads to a decrease in shear strength, stiffness, and energy dissipation capacity. A common solution to prevent the buckling of the wall is to add stiffeners to the steel plate. The involvement of stiffeners, however, obviously results in additional fabrication cost. In addition, steel shear walls usually develop relatively large inelastic deformation and as a result, the connections of the boundary frame can undergo relatively large cyclic rotation.

Composite steel concrete shear walls combine the best characteristics these two construction materials have to offer, which can be one of the alternatives for new forms of structural systems that have high shear strength and deformation capacity under large axial compressive load and cyclic lateral force. These composite walls can be classified into two categories. The first category is the so-called steel-encased concrete composite walls which have steel embedded in the concrete walls [9–10]. The second consists of double plates as the outside face and in-filled concrete walls, namely concrete-filled double-steel-plate composite walls [11–13]. In addition, a new system comprising steel boundary and in-filled concrete [14–15] is considered as an alternative to the traditional composite walls. Extensive research indicates that these composite walls offer excellent structural advantages, particularly in terms of high strength, good stiffness, large deformation capacity, and fast energy dissipation.

In this paper, an innovative shear wall, namely bundled lipped channel–concrete (BLC–C) composite wall, is proposed. Several cold-formed lipped channels were connected by full penetration welds, serving as the frame of the wall. Concrete is poured inside to act compositely with the steel. Therefore, such a cross-sectional arrangement of the composite wall is expected to enhance the seismic behavior of the wall while reducing the amount of steel consumption. Furthermore, this composite wall system is designed to resist both the vertical load and the lateral load, which is quite different from most of the previous wall systems that act as lateral-force resisting systems only. The structural capacity of the proposed composite walls was investigated

through a series of cyclic tests on seven specimens. The seismic behavior of the walls was evaluated in terms of failure modes, hysteresis loops, strength, stiffness, deformation, ductility, and energy dissipation capacity.

2. Experimental program

2.1. Specimen design

The test specimens were designed to simulate the structural walls of the high-rise buildings. Seven full-scaled BLC–C composite walls labeled from BLC–C-1 to BLC–C-7 were tested under quasi-static cyclic loading to investigate the seismic performance of the proposed walls. The geometric detail of the BLC–C composite walls is provided in Fig. 1 and Table 1. The height of all the specimens are identical ($=2700$ mm). All specimens are filled with concrete inside. The parameters studied in this research include the configuration of the wall, the axial force ratio, the presence of the shear studs, and the loading history.

Specimens BLC–C-1 and BLC–C-2 have identical properties except that the axial force ratios for Specimen BLC–C-1 and BLC–C-2 are 0.4 and 0.7, respectively. The specimens with a cross-section of 1324 mm × 130 mm consists of two 160 mm × 130 mm × 4 mm lipped channels at the two boundaries and five 200 mm × 130 mm × 4 mm lipped channels in the middle as given in Fig. 1(a). The adjacent channels are connected by complete joint penetration (CJP) welds along the seams. A steel sheet with the thickness of 4 mm was used in the middle of the wall where no vertical stiffener exists and thus, the BLC–C composite wall is divided into several compartments by the webs of the channels and the sheet. In order to facilitate the filling of concrete inside, a series of 45 mm × 80 mm slot holes are drilled in advance on both the webs of the channels and the steel sheet. The detailed location and dimension of the holes is illustrated in Fig. 1(h).

Specimens -3, -4 and -5 are all composed of nine lipped channels with the cross-sectional size of 160 mm × 130 mm × 4 mm (see Fig. 1(b)). Specimen -3 is subjected to an axial force ratio of 0.4, while the other two are applied to an axial force ratio of 0.6. In addition, staggered welded shear studs are arranged in the inner sides of the webs of two boundary-channels at the center to center vertical spacing of 300 mm as specified in Fig. 1(f)–(g). It should be noted that the shear studs are welded to the lipped channels before the wall is formed in order to facilitate construction. Specimen -6 has nine 120 mm × 130 mm × 3 mm lipped channels in the middle and two 200 mm × 130 mm × 5 mm lipped channels as the boundary as depicted in Fig. 1(d). Specimen -7 is fabricated by welding twelve 160 mm × 130 mm × 4 mm lipped channels together as shown in Fig. 1(e).

2.2. Material properties

The concrete used in the specimens has a strength grade of C40 (nominal cubic compressive strength $f_{cu,d} = 40$ MPa, and designed value of axial compressive strength $f_{c,d} = 19.1$ MPa). Six cubes of 150 mm size was fabricated and cured for 28 days. The tested actual cubic compressive strength $f_{cu,t}$ is 47.11 MPa. It should be noted that the axial compressive strength of concrete $f_{c,t}$ is taken as $0.76f_{cu,t}$ according to the Chinese Code for Design of Concrete Structures GB 50010-2010 [16].

Cold-formed steel is used for the structural steel. Three tensile coupons per thickness cut from the sheets were tested to determine the yield strength (f_y), the ultimate tensile strength (f_u), the yield ratio (f_y/f_u) and the elongation ($Elo.$). The experimental results related to steel properties are given in Table 2.

2.3. Test setup and loading procedure

The specimens were tested by the 20,000 kN multi-functional loading device in Tsinghua University. The vertical and the horizontal loading capacities of the device were 20,000 kN and 3500 kN, respectively. The general arrangement of the test setup is illustrated in Fig. 2. The specimen was placed in a steel loading frame. In order to enhance the connecting parts and prevent the fracture of the welds during the loading process, steel sheets with a width of 50 mm and a thickness of 6 mm were welded around the top and bottom of the wall. Additionally, two end plates with a thickness of 60 mm and 40 mm, respectively, were connected to the bottom and top of the wall by full penetration welds. The bottom plate and top end plates were bolted to the foundation beam and the top beam, respectively. The foundation beam was clamped to the reaction floor by ground anchor. The top beam was clamped to two hydraulic actuators, both in the horizontal directions. The hydraulic actuator in the vertical direction was fixed in the loading frame and meanwhile, was simply placed on the top beam. The friction between the vertical actuator and the top beam, which accompanies with the cyclically changing horizontal displacement during the test, was subtracted from the total horizontal (lateral) force provided by the horizontal actuators to obtain the actual lateral force on the specimen. The was achieved by using the strain cell in the loading device to measure the strain change which can in addition, be converted to the frictional force. The cylindrical bearing in the vertical actuator prevented itself from burdening the moment that might be induced by the friction.

All specimens were tested under constant vertical load (axial force) and cyclically increasing horizontal load. The axial force was applied to the specimen initially by the vertical hydraulic actuator and maintained constantly for the duration of the test. Afterwards, cyclic lateral force was applied by the two horizontal actuators mounted horizontally to the steel columns of the loading frame.

The axial force ratio would largely affect the height of compression zone and the deformation capacity of the walls. It is considered as an extremely essential factor in designing the test. The axial force ratio is derived from Eq. (1),

$$n_d = \frac{N}{f_{c,d}A_c + f_{y,d}A_s} \tag{1}$$

where n_d = axial force ratio without the web; n_{d1} = axial force ratio with the web; N = axial compressive force applied by the vertical hydraulic actuator; $f_{c,d}$ = compressive strength of concrete, which can be calculated from the cubic compressive strength as mentioned in Section 2.2; $f_{y,d}$ = yield strength of steel sheet; A_c and A_s = cross-sectional area of the concrete and steel, respectively. It should be noted that the webs of the lipped channels inside the wall were used as the safety reserve. Their contributions to either the overall strength of the wall or the calculation of axial force ratio were not taken into account.

The lateral cyclic loading history was generally based on the testing protocol specified in the Chinese Specification of Testing Methods for Earthquake Resistant Building (JGJ 101-96) [17]. Before the specimen yielded, the lateral force was controlled by load. In the load-controlled stage, lateral force was applied in five levels, which corresponded to 1/5, 2/5, 3/5, 4/5, and 1 of the predicted yield strength of the specimen. The lateral force was changed to displacement-controlled after the specimen yielded. The lateral displacement of the wall at the top was monitored by displacement transducers and the yield displacement was defined as D_y. Since then, two types of loading procedures were applied. For Specimens -1 and -2, the displacement increment corresponded to D_y and three cycles were performed for each displacement level as
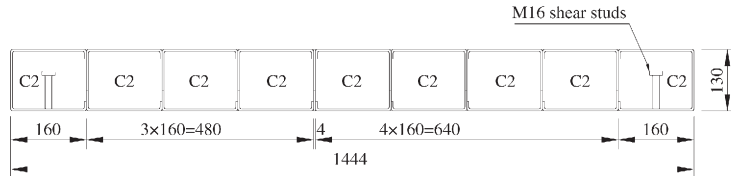
Fig. 1. Configuration details of specimens. (a) Sectional configuration of Specimens -1 and -2. (b) Sectional configuration of Specimens -3 and -4. (c) Sectional configuration of Specimen -5. (d) Sectional configuration of Specimen -6. (e) Sectional configuration of Specimen -7. (f) Front view of Specimen -5. (g) Back view of Specimen -5 (h) 1–1 section.
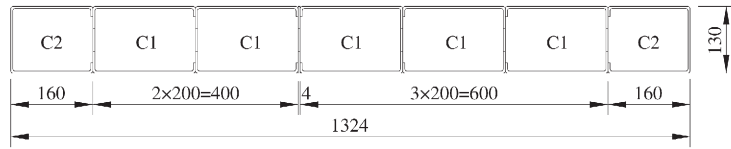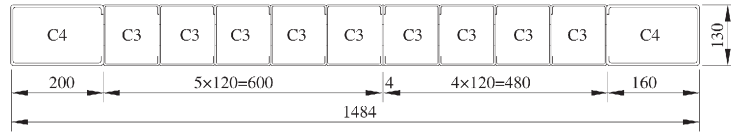
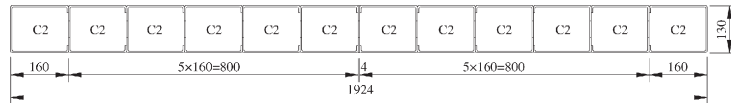(a) Sectional configuration of Specimens BLC-C-1 and BLC-C-2
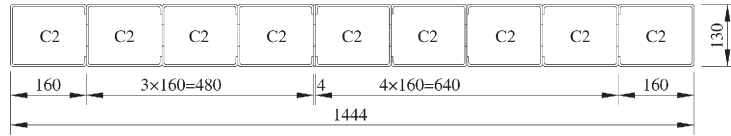
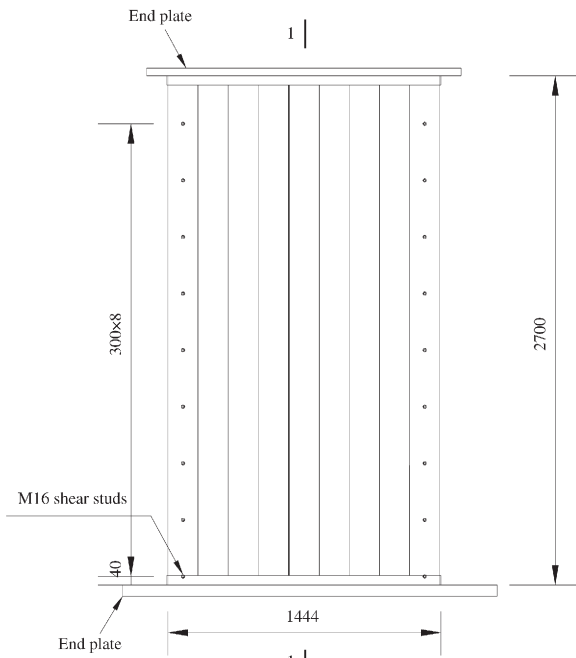(b) Sectional configuration of Specimens BLC-C-3 and BLC-C-4

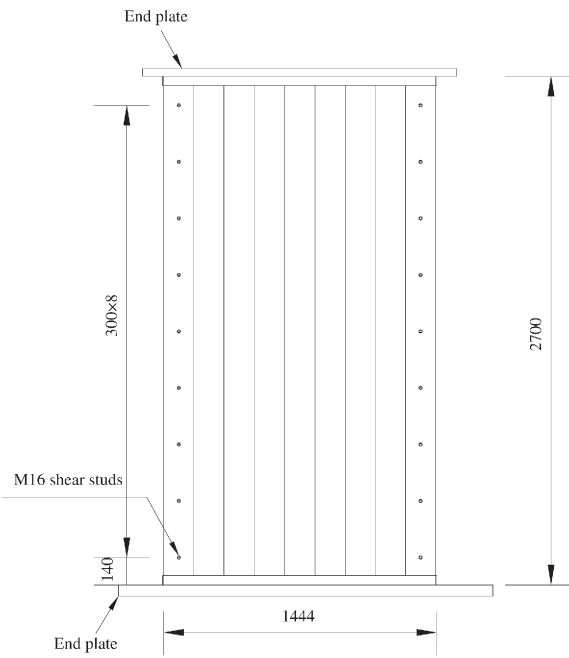(c) Sectional configuration of Specimen BLC-C-5
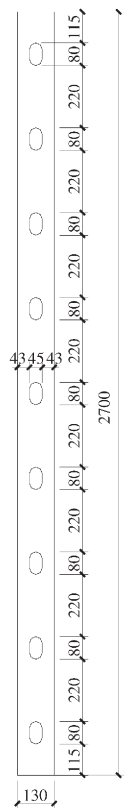
(d) Sectional configuration of Specimen BLC-C-6

(e) Sectional configuration of Specimen BLC-C-7

(f) Front view of Specimen BLC-C-5

(g) Back view of Specimen BLC-C-5

(h) 1-1 section

Table 1
Summary of test specimens.

Specimen No.	Height of wall (mm)	Cross section (mm × mm)	Configuration	Shear studs	Axial load ratio (without the web) n_d	Axial load ratio (with the web) n_{d1}	Axial force kN	Loading history	Steel ratio (%)
-1	2700	1324 × 130	C2 + 5C1 + C2	–	0.4	0.35	2668	Type 1	8.57
-2	2700	1324 × 130	C2 + 5C1 + C2	–	0.7	0.52	4670	Type 1	8.57
-3	2700	1444 × 130	9C2	–	0.4	0.34	2899	Type 2	8.92
-4	2700	1444 × 130	9C2	–	0.6	0.51	4349	Type 2	8.92
-5	2700	1444 × 130	9C2	√	0.6	0.51	4349	Type 2	8.92
-6	2700	1484 × 130	C4 + 9C3 + C4	–	0.6	0.51	4267	Type 2	8.03
-7	2700	1924 × 130	12C2	–	0.6	0.51	5734	Type 2	8.86

Note: C1 denotes the lipped channel with the cross section of 200 mm × 130 mm × 4 mm; C2 denotes the lipped channel with the cross-sectional area of 160 mm × 130 mm × 4 mm; C3 denotes the lipped channel with the cross section of 120 mm × 130 mm × 3 mm; and C4 denotes the lipped channel with the cross section of 200 mm × 130 mm × 5 mm.

shown in Fig. 3(a). For the rest of the specimens, it was loaded at intervals of $0.5D_y$. Namely, the lateral displacement increased in the sequence of D_y, $1.5D_y$, $2D_y$, $2.5D_y$, $3D_y$, $3.5D_y$. Two cycles were repeated at each displacement level. The adopted loading procedure is detailed in Fig. 3(b). In each loading cycle, a push (from the right to the left in Fig. 2) was conducted first, followed by a pull (from the left to the right). The push and the pull were defined as the positive loading and negative loading, respectively. The test was terminated when the axial load on the wall could not be maintained or the lateral force decreased below 85% of the maximum load.

As the face of the specimen was expected to locally deform under cyclic loading, the faces of the specimens were coated with whitewash painting to help observe local buckling and failure mode.

2.4. Instrumentation

The lateral and vertical loads applied on the specimen were automatically recorded by the load cells in the hydraulic actuators. Eleven displacement transducers (DTs) were mounted to measure the global and local deformations of the specimen. DT H-1 was placed at the top with the same height of the loading point to monitor the lateral displacement of the specimen. DTs H-2, H-3 and H-4 measured the lateral displacements along the height of the wall. DTs H-5, V-1, and V-2 were mounted on the foundation beam. DT H-5 was used to measure the horizontal slippage of the foundation beam along the direction of the lateral force, and the other two were applied to measure the rotation that may be caused by the potential uplift of the foundation beam from the reaction floor. DTs H-6 and H-7 were installed to monitor the possible out-of-plane deformation of the specimen. One pair of diagonally arranged DTs H-8 and H-9 was used to measure the shear deformation of the wall. The layout of the displacement transducers is illustrated in Fig. 4.
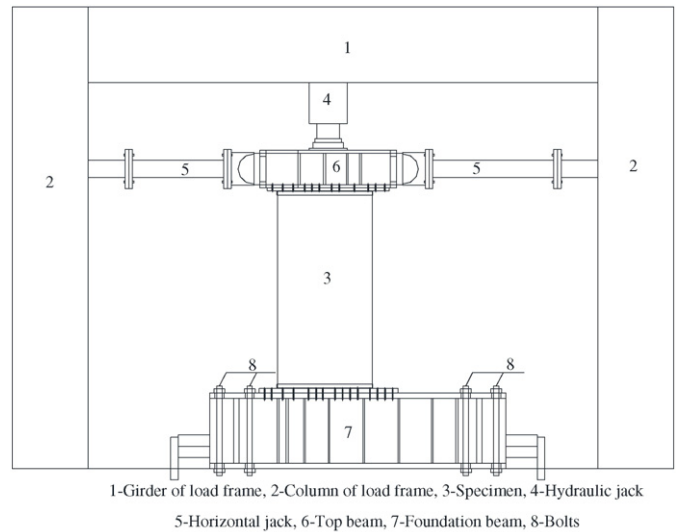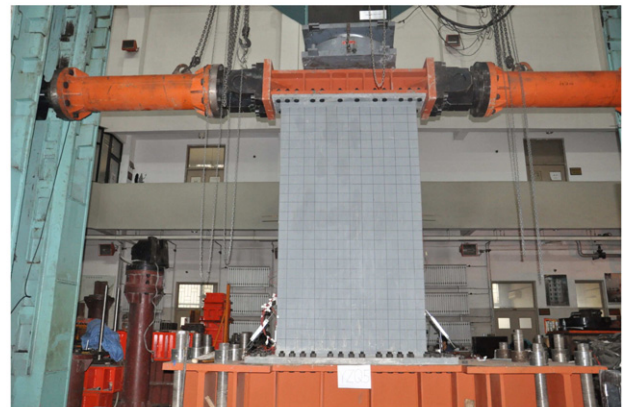
3. Test results

3.1. General behavior

3.1.1. Specimen -1

Specimen -1 behaved almost in an elastic manner up to the lateral displacement of 15 mm (corresponding to the drift of 1/180 rad) and the horizontal force of 886 kN. The load–displacement response of the specimen was essentially linear. Afterwards, yielding began to develop as can be observed from the change in slope of the load–displacement curve. The maximum load of 1024 kN was achieved at the displacement

of 30 mm ($2D_y$, corresponding to the drift of 1/90 rad). Slight sounds were emitted from the specimen and very slight buckling was observed at the height of 150 mm from the bottom of the specimen. During the 3rd cycle of 1/90 rad, local buckling was observed at three different locations. In the loading group of 45 mm displacement ($3D_y$, equaling to the drift of 1/60 rad), the observed horizontal force dropped to 90% of the maximum lateral force. Continuous sounds were emitted and local buckling developed to five locations. It can be found at this level of drift that the contact between the steel and the in-filled concrete was almost gone within a large area at the bottom of the specimen. During the 1st positive loading cycle of the displacement of 60 mm ($4D_y$, drift of 1/45 rad), severe buckling was observed at six locations at the height

1-Girder of load frame, 2-Column of load frame, 3-Specimen, 4-Hydraulic jack
5-Horizontal jack, 6-Top beam, 7-Foundation beam, 8-Bolts

(a) Schematic view

(b) On-site photo

Fig. 2. Test setup. (a) Schematic view. (b) On-site photo.

Table 2
Material properties of steel.

Type	t (mm)	f_y (N/mm^2)	f_u (N/mm^2)	f_y/f_u	Elo. (%)
Steel sheet	3	424.3	498.5	0.85	33.0
	4	433.1	504.8	0.86	32.7
	5	419.0	538.9	0.78	33.6

(a) For Specimens BLC-C-1 and BLC-C-2 (type 1)

(b) For Specimens BLC-C-3 through BLC-C-7 (type 2)
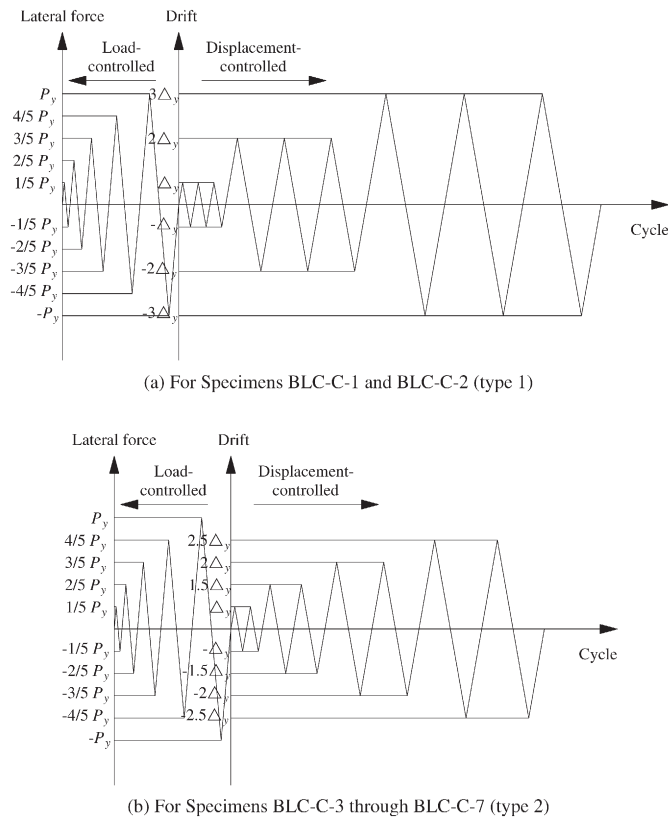
Fig. 3. Loading history. (a) For Specimens -1 and -2. (b) For Specimens -3 through -7.

Fig. 4. Arrangement of displacement transducers.

of 150 mm and 350 mm from the bottom. By the end of the 1st cycle, buckling totally developed around the specimen at the height of 150 mm and 350 mm. After the 2nd cycle of the drift of 1/45 rad, fracture occurred at the bottom of the boundary of the specimen. Simultaneously, the concrete was crushed at the height of 150 mm, as shown in Fig. 5(a). Small fractures were observed on the other side as seen in Fig. 5(b). A horizontal crack also developed in the CJP weld that was used to connect the adjacent lipped channels. The lateral force was reduced to 70% of the maximum capacity of the specimen, and the specimen was considered failed. The test stopped. The failure photograph of Specimen -1 is shown in Fig. 5(c).

3.1.2. Specimen -2

For Specimen -2, the axial force ratio of 0.7 was applied. In the process of applying the vertical load, slight sound could be heard at the axial vertical force level of 3500 kN. No physical phenomenon was observed at this stage. The sound became larger when the vertical load arrived at 4000 kN. It was found that slight buckling had occurred at the bottom of the specimen, which means that the specimen had begun to develop yielding under such high axial force ratio. The predicted yield shear force of 794 kN was considered as the yield strength, and the corresponding lateral displacement of 14 mm was regarded as the yield displacement. It should be noted that the defined yield strength in the process of this experiment differs from the actual yield strength that was determined in the analyses. In the loading group of 14 mm displacement, no apparent deformation was observed. During the 1st positive loading cycle of the displacement of 28 mm ($2D_y$), some slight buckling occurred at the height of 150 mm and 300 mm from the base. In the 2nd positive loading cycle, five locations near the base developed local buckling when the lateral force reached 985 kN. One more location began to buckle during the 2nd negative loading cycle. At the 3rd negative loading cycle, the specimen had noticeable local buckling at the height of 300 mm and the steel sheet dwelled out for about 2 mm in maximum, as shown in Fig. 6(a) and (b). The force–
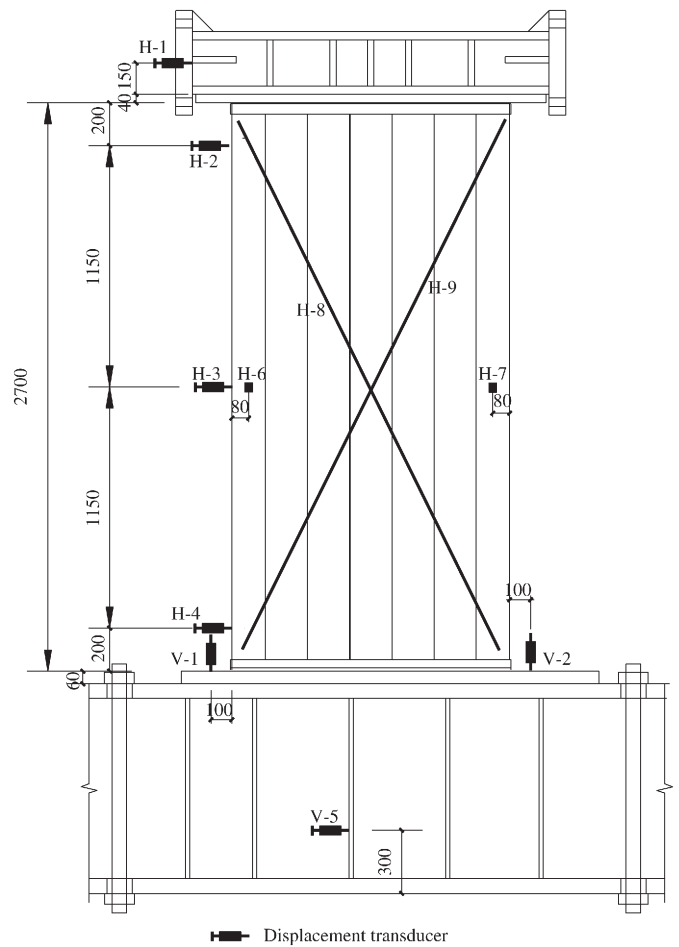
displacement curve began to drop when the lateral force was around 850 kN in the 1st positive cycle of the 42 mm displacement ($3D_y$). The specimen heavily buckled near the base of the wall. During the 1st negative cycle of the same displacement level, the recorded lateral force apparently decreased. The load had dropped to 500 kN when the lateral displacement was just over 30 mm. The test was terminated in order to prevent the damage to the test setup. The failure condition is shown in Fig. 6(c).

3.1.3. Specimen -3

Specimen -3 had an axial force ratio of 0.4. The levels of the vertical axial load were considered in three phases, which were 20%, 50%, and 100% of the designed axial load. No obvious buckling or any other sign was seen during this stage. A slight sound was heard from four locations which were labeled by the white tapes as shown in Fig. 7(a). A more continuous sound was emitted from the locations labeled as red in Fig. 7(a) when the horizontal load arrived at 600 kN. This may be caused by the contact gone between the steel sheets and the concrete. The lateral displacement of 12 mm was defined as the yield deformation of the specimen in the test and the corresponding load was 856 kN. During the displacement level of 12 mm (D_y) and 18 mm ($1.5D_y$, corresponding load of 1097 kN), no physical buckling could be seen, but a heavy sound came from the locations labeled by blue tapes in Fig. 7(a). In the loading group of 24 mm ($2D_y$) with the load level of 1229 kN, the specimen had very slight buckling at two positions near the base. The buckling became more obvious and spread to three locations at the displacement level of 30 mm ($2.5D_y$) with the load of 1309 kN. The buckling was increasingly severe with an increase in the displacement level. The peak load of 1342 kN was reached at the displacement of

(a) Severe buckling and concrete crushing

(b) Horizontal crack in the weld

(c) Failure photo

Fig. 5. Failure of Specimen -1. (a) Severe buckling and concrete crushing. (b) Horizontal crack in the weld. (c) Failure photo.

(a) Local buckling from the side view

(b) Local buckling from the front view

(c) Failure condition

Fig. 6. Failure of Specimen -2. (a) Local buckling from the side view. (b) Local buckling from the front view. (c) Failure condition.

30 mm ($3.0D_y$). In the 1st loading group of 42 mm displacement ($3.5D_y$) with the lateral load of 1280 kN, two locations 150 mm above the base of the specimen heavily buckled. At the 1st positive loading cycle of the displacement level of 48 mm ($4D_y$) with the corresponding horizontal load of 1202 kN, the left three lipped channels of the wall had severe buckling. Simultaneously, fracture occurred 150 mm from the base of the wall at the right boundary and quickly propagated the full depth of the wall as detailed in Fig. 7(b). When the lateral displacement reached 20 mm of the 2nd positive cycle, five buckled waves were

observed at the left part of the specimen at a 150 mm height from the base. The fracture on the other side developed to a length of 130 mm. During the lateral displacement of 54 mm ($4.5D_y$), when the displacement arrived at 13 mm, a distinctive sound was heard. Another two sounds were emitted as the displacement reached 40 mm. The length of the fracture near the right base increased to 150 mm. Another two cracks were found at the right side, one located 160 mm from the right boundary with the length of 50 mm and width of 20 mm, and the other small one located 320 mm from the right. Three small fractures were also observed near the left boundary of the specimen as shown in Fig. 7(c). The test stopped as the lateral load dropped to 866 kN, which was less than 80% of the maximum force capacity.

(a) Locations of labeled tapes

(b) Fracture propagation
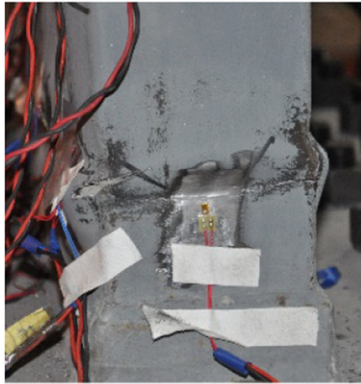
(c) Small fractures observed

Fig. 7. Failure of Specimen -3. (a) Locations of labeled tapes. (b) Fracture propagation. (c) Small fractures observed.

3.1.4. Specimen -4

Specimen -4 exhibited a stable hysteretic curve at an early stage. At the displacement of 10 mm, no apparent deformation occurred. However, 10 mm was defined as the predicted yield displacement (D_y) for the rest of the specimens for convenience. In the loading group of 20 mm displacement ($2D_y$), a slight buckling was found at two boundaries at 150 mm height from the base. The horizontal load reached its maximum value of 1259 kN at the displacement level of 30 mm ($3.0D_y$). The two adjacent lipped channels at two boundaries exhibited moderate

buckling. At further cycles after the peak load, more buckling was observed (see Fig. 8(a)). At the 1st cycle of the displacement group of 45 mm ($4.5D_y$), the lateral force decreased to 885 kN. The local buckling was extended to ten locations. During the 2nd cycle of the 45 mm, the load dropped to 753 kN. There was local buckling around the wall in the horizontal direction at the height of 150 mm up from the base, as can be seen from Fig. 8(b). The specimen was considered failed as the fracture that initiated from the corner ran through the depth of the specimen.

3.1.5. Specimen -5

For Specimen -5, the vertical load was applied in five stages. A slight sound was emitted from the specimen (the regions were labeled by blue tapes in Fig. 9(a)) when the axial force arrived at 4000 kN. The locations where the sound was heard under the axial force of 4350 kN were marked by red tapes. Out-of-plane deformation of 6 mm was observed after the vertical load was completed. The specimen still remained elastic before the horizontal displacement of 10 mm. In the loading group of 10 mm displacement, the specimen yielded but there was no sign of buckling on the wall. At the lateral displacement of

(a) Local buckling
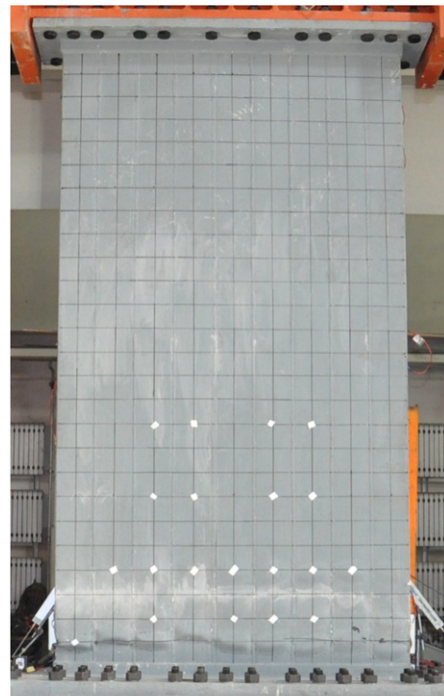
(b) Buckling around the wall

Fig. 8. Failure of Specimen -4. (a) Local buckling. (b) Buckling around the wall.

20 mm ($2D_y$), the out-of-plane deformation increased to 12 mm. The deformation continued to grow up and reached 16 mm during the lateral displacement of 25 mm ($2.5D_y$). Simultaneously, the channel at the boundary showed very slight buckling at 150 mm up from the base. During the displacement of 30 mm ($3.0D_y$), the load arrived at its maximum value of 1236 kN. In the cycle of 35 mm displacement ($3.5D_y$), the wall deformed 30 mm out of the plane at the height of 1350 mm. The existing local buckling at the height of 150 mm was aggravated and new buckling was observed at eight more regions. The most obvious buckling was observed 250 mm from the base as shown in Fig. 9(b). During the positive cycle of 40 mm ($4D_y$) displacement, the lateral force dropped to 862 kN. The out-of-plane deflection at the height of 1300 mm increased to 51 mm. Buckling was observed at nine regions located at the height of 150 mm, 250 mm, and 450 mm. In the 2nd cycle as the lateral displacement reached 22 mm, the wall deformed out 73 mm at the wall center (see Fig. 9(c)). The horizontal load decreased to 80% of the peak load and the test stopped.

3.1.6. Specimen -6

Specimen -6 was applied to the vertical axial load of 4270 kN. As the horizontal load reached 400 kN, a continuous slight sound was emitted from the regions that were marked by red tapes in Fig. 10(a). The lateral displacement of 10 mm was defined as yield displacement and the corresponding horizontal load was 914 kN. No obvious deformation was noticed until the displacement reached 25 mm ($2.5D_y$). The boundary exhibited small buckling at 150 mm from the base as shown in Fig. 10(b), which was similar to the other specimens. At further cycles the buckling became more noticeable and more areas suffered from buckling. The peak load of 1439 kN was achieved in the loading group of 30 mm displacement ($3D_y$). At the displacement of 35 mm ($3.5D_y$), local buckling was observed at six positions located at the height of 150 mm and 350 mm from the base. However, there was no buckling seen at the corner of the wall. Concrete crushing was observed at the boundary. During the displacement of 45 mm ($4.5D_y$), the buckling developed to eight locations and the in-filled concrete from the base up to 250 mm got crushed. In the 2nd cycle of 50 mm ($5D_y$) displacement, the region from the base to the height of 350 mm completely suffered from buckling. The fracture occurred at the corner of the wall and quickly developed to the depth of the specimen along the horizontal direction. The test was terminated.

3.1.7. Specimen -7

For Specimen -7, the buckling was first observed at 250 mm up from the base in the loading group of 20 mm ($2D_y$) displacement. At the displacement of 25 mm ($2.5D_y$), local buckling was extended to seven regions located at the height of 150 mm, 250 mm, and 350 mm. When the displacement arrived at 30 mm ($3D_y$), the ultimate lateral load was 2230 kN. Concrete crushing was observed at the two adjacent channels at the boundary. During the loading displacement of 45 mm ($4.5D_y$), concrete below the height of 450 mm completely got crushed. The fracture initiated at the corner of the wall. When the displacement reached 50 mm ($5D_y$) and the lateral load was 1603 kN, the fracture significantly developed at the height of 150 mm at the corner as shown in Fig. 11(a). Severe buckling was observed at several horizontal lines (see Fig. 11(b)) and the specimen also suffered from a twist. The test stopped. The failure of the specimen is shown in Fig. 11(c).

3.2. Damage and failure mode

As can been seen from the detailed description in Section 3.1, all the specimens experienced similar damage patterns, which include the local buckling of the steel sheets, and the fracture propagation of the steel sheets at the base of the wall. The damage process can be identified as three major stages: the elastic stage, the yielding developing stage, and the failure stage. The phenomenon observed in each stage is summarized below.

The elastic stage started from the onset of the test until the yields occur in the specimens. The specimens showed almost an elastic manner in this stage. The horizontal force increased linearly with an increase in the lateral displacement. No local buckling or any other physical deformation was observed.

The yielding developing stage began from the yielding to reaching the ultimate strength of the specimens. The walls first had slight buckling at the base of the boundary corners. The local buckling became more obvious and spread to more areas upon further loading.

The failure stage stated from the ultimate load to the failure of the specimens. As the further lateral displacement progressed, the existing local buckling of the steel sheets was greatly developed and aggravated. New buckling was observed at more locations. The local buckling was located from the base of the wall up to a height of 450 mm. The concrete inside got crushed at further cycles. Tensile fracture along the horizontal direction initiated at the corner of the wall and quickly propagated across the depth of the specimen. Finally, the specimen lost its capacity to maintain the horizontal load and suffered a complete failure.

4. Analysis and discussion

4.1. Force–displacement response

The performance of the shear wall is critically important to the response of composite frame, and is largely dependent on the force versus displacement relationship. The lateral force and the corresponding displacement at the top of the wall was used to construct the hysteresis force–displacement curve of the test specimens shown in Fig. 12, where the lateral force is recorded by the load cell in the hydraulic actuator, and the top displacement is measured by the displacement transducer at the top of the specimen.

The hysteresis loops exhibited ductility. The shapes of the curves were stable and plentiful without a noticeable pinching effect. The following conclusions can be drawn:

1. More intensive loops can be observed in Specimens -3 to -7 than in Specimens -1 and -2. This is caused by the different loading histories. An interval of $1D_y$ was imposed to Specimens -1 and -2 while an increment of $0.5D_y$ was applied to the rest of the specimens.

2. The axial load ratio affects the shape of the hysteresis loops. Lower axial force ratio in Specimen -1 than -2 leads to more stable behavior exhibited in the former specimen. A similar phenomenon can be observed when comparison is made among Specimens -3, -4, and -5.

3. Specimen -6 had the most plentiful hysteresis loops. This can be explained by the fact that the boundary of the wall is reinforced by the lipped channel with a stronger cross section of 120 mm × 130 mm × 5 mm, which means more stable and ductile performance can be achieved by stiffening the boundary zone. This is logical and expected as the boundary zone of the wall suffers to a larger moment-induced axial force when subjected to horizontal load.

4. Comparison among Specimens -2, -4 and -6 indicates that for the wall with a certain length, adopting lipped channels with a smaller cross-sectional area in the wall body leads to more "webs" inside the specimen, which in turn, results in a more intensive arrangement of transverse vertical stiffeners. Therefore, a more stable performance can be achieved.

5. The impact of the welded shear studs to the entire structural behavior of the specimen can be ignored. It is found that the responses of Specimens -4 and -5 were fare before failure occurred, as evidenced by the shape of hysteresis loops. However, Specimen -5 failed at a smaller displacement level. This unexpected phenomenon may be caused by the out-of-plane deformation which reduces the ductility of the wall. It should be noted that the presence of shear studs does affect the damage pattern of the specimen and delay the occurrence of fracture and failure as well. For Specimen -4, the local buckling at the boundary was observed in the loading group of 20 mm displacement,
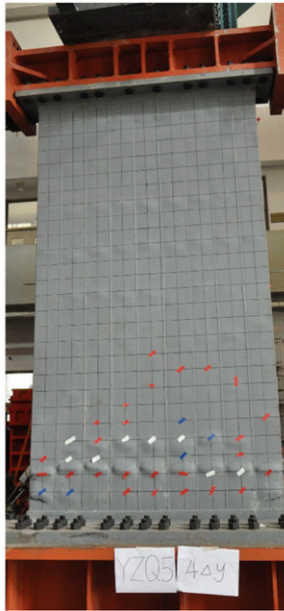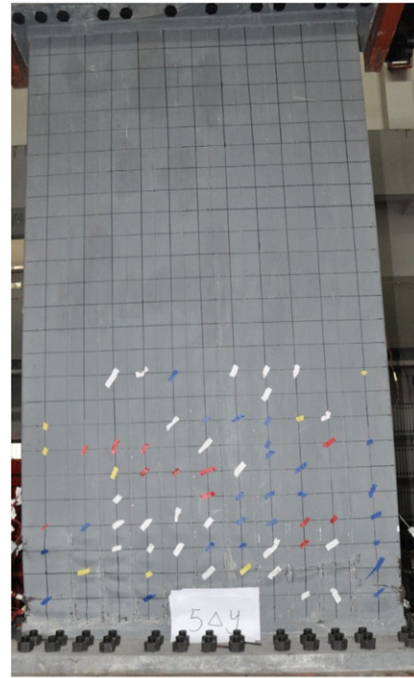
(a) Locations of labeled tapes and the failure condition
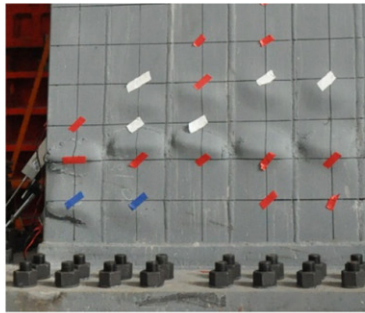
(b) Local buckling

(c) Out-of-plane deformation


(a) Failure and the labelled location

(b) Local buckling

Fig. 10. Failure of Specimen -6. (a) Failure and the labeled location. (b) Local buckling.

while it was at the displacement of 25 mm for Specimen -5. Additionally, concrete crushing initiated at the boundary of Specimen -4 while it was first observed at the wall body around 240 mm away from the corner for Specimen -5. Furthermore, shear studs prevent the steel sheets from buckling and help the steel and concrete act compositely under loading. As can be seen in Fig. 9(a), no local buckling was observed at the location with shear studs right inside. In contrast, the steel sheets without shear studs severely buckled at the same height.

In order to compare the peak load, initial stiffness, ductility capacity and energy dissipation capacity of the specimens, the force–displacement hysteresis curve was converted to the equivalent force–displacement envelope curve. As mentioned by Qin et al. [18], the concept of an envelope curve has been widely adopted in Japan in characterizing the deformation of structural members subjected to reversal load.

Fig. 9. Failure of Specimen -5. (a) Locations of labeled tapes and the failure condition. (b) Local buckling. (c) Out-of-plane deformation.

(a) The developed fracture

(b) Buckling development

(c) Failure condition
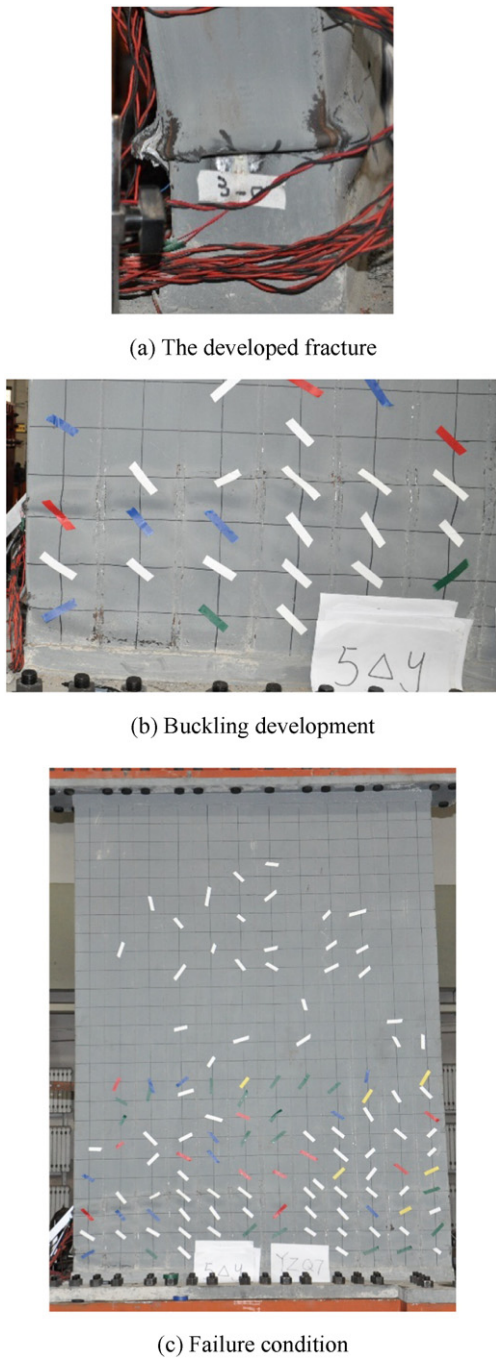
Fig. 11. Failure of Specimen -7. (a) The developed fracture. (b) Buckling development. (c) Failure condition.

Hysteresis loops were expected to increase their displacement range at further cycles. When the force during the following cycle exceeds the peak load on the previous cycle, the exceeding portion of the loop during the following cycle is connected to the point at the peak load of the previous cycle. The same process is repeated until the failure point is reached. In this procedure, an envelope curve was defined and constructed for each of the positive and negative loading directions as given in Fig. 13. The test value obtained for initial stiffness, yield load and peak load are summarized in Table 3. The method to determine the yield strength of the specimen is illustrated in Fig. 14.

It can be observed that the performance of the specimens was initially elastic, followed by an inelastic behavior with gradually degrading

stiffness, until the failure occurred. In general, the structural behavior of the specimens with the same cross section is similar. However, the load–displacement curve sharply dropped to failure point after the peak load was achieved for specimens with high axial force ratio. This means that a high axial force ratio would restrain the deformation capacity of the specimen. It should be mentioned that a quicker drop in the negative semi-portion occurs in Specimen -5 than in -4. This is because the out-of-plane deformation of Specimen -5 leads to an extra moment on the wall and results in a poorer deformation capacity. In addition, the most moderate degrading was observed in Specimen -6, as shown in Fig. 13(d), due to the enhancing boundary and most intensive arrangement of inside "webs" (or transverse vertical stiffeners).

The cross-sectional area contributes most to both the yield horizontal strength and the peak lateral load while the impact of the axial force ratio and the loading history are negligible. The yield strengths and peak loads for Specimens -1 and -2 are relatively low due to the small cross section. The positive yield and ultimate lateral forces for Specimen -7 reached as high as 1897 kN and 2320 kN, respectively, because of the largest cross-sectional area of the wall. However, only a slight difference can be noticed among specimens with the same cross section subjected to different axial load ratios or loading procedures.

The initial stiffness is affected by both the cross-sectional area and the axial load ratio. The values of initial stiffness for all specimens are listed in Table 3. The specimen with either a larger cross-sectional area or lower axial load ratio offers higher stiffness. The positive initial stiffness increases from 72,943 kN/m for Specimen -1 to 77,043 kN/m for Specimen -3 as the cross-sectional area increases from 2700 mm × 1324 mm to 2700 mm × 1444 mm. Meanwhile, a 9436 kN/m decrease (corresponding to a 12.9% drop) in positive initial stiffness is observed as the axial force grew up from 0.4 for Specimen -1 to 0.7 for Specimen -2.

The comparison with steel tube–double steel plate–concrete composite walls [15] shows that the yield rotation of composite walls is close to that of steel tube–double steel plate–concrete composite walls, while the ultimate rotation of the former is significant larger than that of the latter. Meanwhile, the comparison with concrete filled double-steel-plate (CFDSP) composite wall [19] indicates that both the yield and ultimate rotation of these two wall systems are almost the same. This demonstrates that the performance of the proposed composite walls is superior to that of steel tube–double steel plate–concrete composite walls and meanwhile, is close to that of CFDSP composite walls.

4.2. Strength degradation

Strength degradation is a key element to evaluate the performance of strength under cyclic loadings such as earthquake ground motions. It is evaluated by using the strength degradation ratio (η_i), which is defined as the ratio of the maximum strength in the last cycle to that in the first cycle at the same displacement level, as given in Eq. (2),

$$\eta_i = \frac{P_i^n}{P_i^1} \tag{2}$$

where n is the number of cycles at the displacement of i. P_i^j is the maximum strength of the jth cycle at the displacement of i.

Fig. 15 plots the values of η_i at different displacement levels for all specimens. It can be observed that η_i gradually decreases with the increase in the displacement level. The strength deterioration is more noticeable as the further cycles progressed. Before the peak load is reached, η_i generally ranges from 0.90 to 0.95 for Specimens -1 and -2 and from 0.95–1.0 for the rest of the specimens, and occasionally exceeds 1.0 for the deviation of measurement, which indicates moderate strength degradation before the maximum strength point. After the peak load is achieved, the strength degradation is more severe and evident. η_i decreases to 0.8 for Specimen -1 and 0.9 for Specimens -3 to -7.
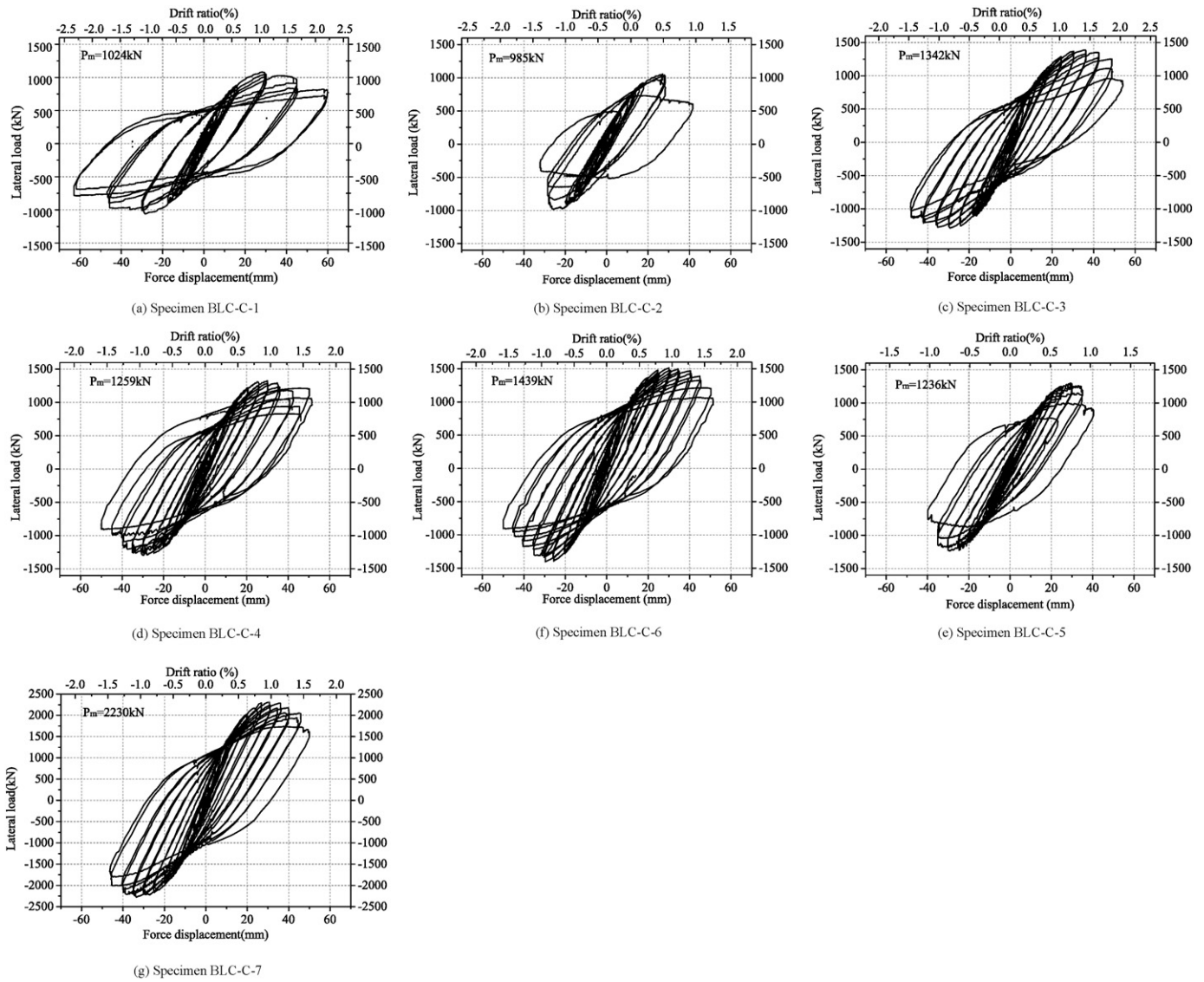
Fig. 12. Hysteresis loops of lateral force versus top displacement relationships. (a) Specimen -1. (b) Specimen -2. (c) Specimen -3. (d) Specimen -4. (e) Specimen -5. (f) Specimen -6. (g) Specimen -7.

η_i is even below 0.65 for Specimen -2 during the negative loading cycles. This is because the highest axial ratio (=0.7) is applied to Specimen -2, which induces the largest deformation at the same displacement level. More severe and intensive local buckling was observed during the test in Specimen -2 than in other specimens by the end of the 3rd cycle in the displacement of $2D_y$, which results in more severe strength degradation. Specimen -6, with the relatively reinforced boundary element, shows much more gradual strength deterioration than the other specimens.

4.3. Stiffness degradation

During the cyclic test, the stiffness of the specimens decreases due to the cumulative damnification. Specimens with a large degree of stiffness degradation tend to exhibit larger deformation under reversal loads and, thus, may lead to extensive damage to other structural members. Stiffness (K_i) is defined as the ratio of the averaged maximum strength to the corresponding averaged lateral displacement at a displacement of i as shown in Eq. (3). Consequently, the stiffness represents the averaged scant stiffness of the specimen at different displacement levels.

Stiffness degradation (ξ) is the ratio of scant stiffness at displacement of i (K_i) to the initial stiffness (K_0) as shown in Eq. (4).

$$K_i = \frac{\sum_{j=1}^{n} F_i^j}{\sum_{j=1}^{n} d_i^j} \tag{3}$$

$$\xi = \frac{K_i}{K_0} \tag{4}$$

where F_i^j is the maximum lateral load of the jth cycle at the displacement of i; d_i^j is the recorded corresponding displacement of the jth cycle at the displacement of i.

The K_i-d curves and ξ-d curves of all specimens are shown in Fig. 16 and Fig. 17, respectively. The cyclic stiffness degradation responses are compared, and the following observations can be made:

1. All specimens have almost identical stiffness degradation behavior. This indicates that the stiffness degradation is not significantly influenced by the specimen configuration. Slight differences can be
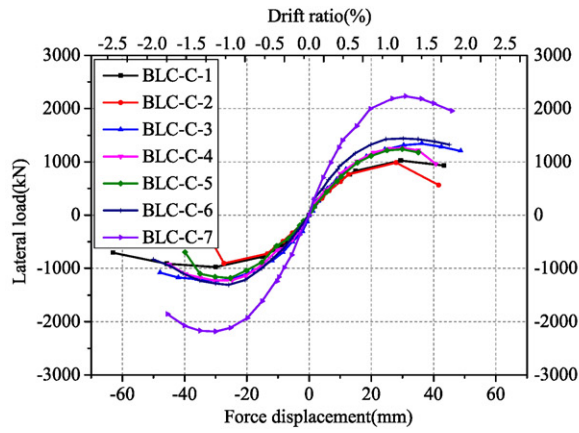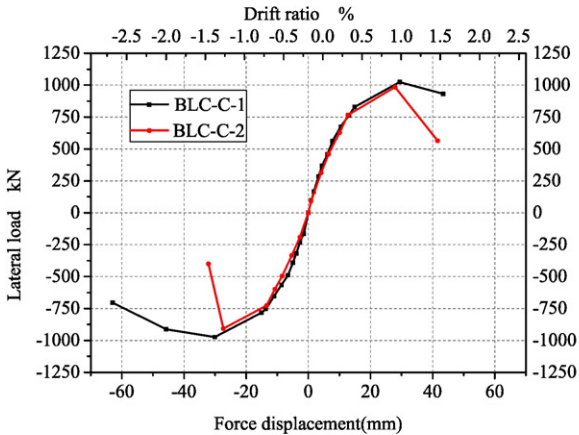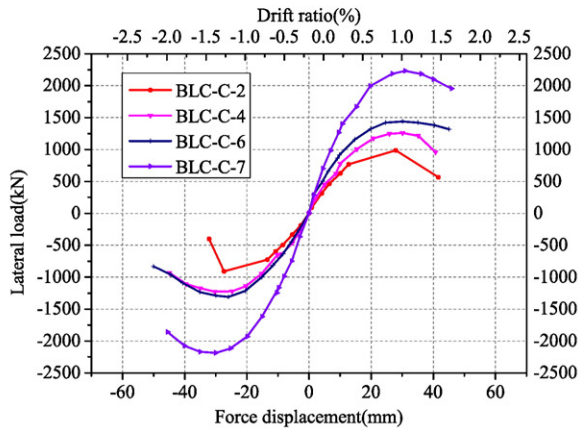
(a) Curves for all specimens
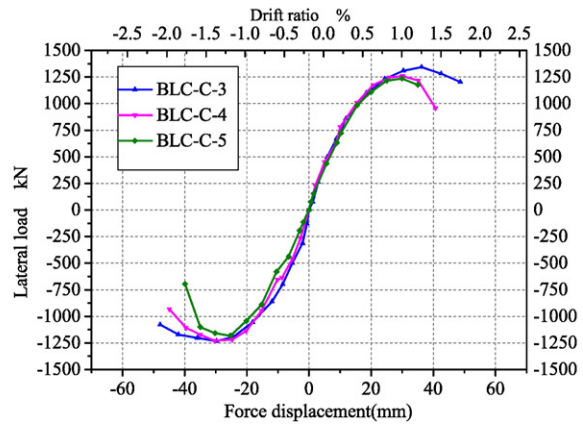
(c) Comparison among Specimens BLC-C-3 through BLC-C-5

(b) Comparison between Specimens BLC-C-1 and BLC-C-2

(d) Comparison among Specimens BLC-C-2, BLC-C-4, BLC-C-6, and BLC-C-7

Fig. 13. Envelope curves of lateral force versus top displacement. (a) Curves for all specimens. (b) Comparison between Specimens -1 and -2. (c) Comparison among Specimens -3 through -5. (d) Comparison among Specimens -2, -4, -6, and -7.

observed among specimens with various axial load ratios. Stiffness deterioration is more stable and gradual in Specimen -3 than in Specimens -4 and -5. The same observation can be found in the comparison between Specimens -1 and -2. This demonstrates that lower axial force ratio offers more stable stiffness degradation pattern.

2. Considerable reduction in stiffness is observed in all specimens as larger lateral displacement is imposed. At the ultimate displacement level, the ratios of the cyclic stiffness to the calculated initial stiffness

for all specimens range from 0.15 to 0.32. It should be noted that before the specimen yields, stiffness degradation ξ for some specimens unexpectedly exceeds 1.0. This is because the initial stiffness K_0 is calculated from the ratio of the averaged lateral load to the averaged lateral displacement before the yielding of the specimen to alleviate the deviation of measurement. At a small displacement level, the calculated stiffness may noticeably differ from its actual value as a relatively large measure deviation.

Table 3
Summary of test results.

Specimen	Loading direction	Initial stiffness (kN/m)	Yield load P_y (kN)	Yield displacement d_y (mm)	Yield drift (rad)	Peak load P_m (kN)	Displacement at peak load d_m (mm)	Drift at peak load (rad)	Ultimate displacement d_u (mm)	Ultimate drift (rad)	Ductility μ	P_m/P_y
-1	(+)	72,943	850	16.7	0.0062	1024	29.5	0.0109	49.6	0.0184	2.98	1.21
	(−)	68,254	789	15.6	0.0058	974	30.0	0.0111	52.9	0.0196	3.39	1.23
-2	(+)	63,507	806	16.4	0.0061	985	28.0	0.0104	32.9	0.0122	2.01	1.22
	(−)	57,600	705	15.5	0.0057	908	27.4	0.0101	28.9	0.0107	1.86	1.29
-3	(+)	77,043	1130	20.3	0.0075	1342	36.3	0.0134	49.9	0.0185	2.46	1.19
	(−)	84,604	910	14.9	0.0055	1233	29.8	0.0110	48.1	0.0178	3.22	1.36
-4	(+)	74,071	1049	16.4	0.0061	1259	30.1	0.0111	42.8	0.0159	2.61	1.20
	(−)	75,646	880	19.6	0.0073	1228	30.3	0.0112	41.8	0.0155	2.13	1.40
-5	(+)	71,678	1099	19.7	0.0073	1236	30.0	0.0111	37.3	0.0138	1.89	1.12
	(−)	64,877	1047	20.1	0.0074	1182	25.3	0.0094	36.2	0.0134	1.80	1.13
-6	(+)	95,075	1202	16.3	0.0060	1440	30.2	0.0112	47.6	0.0176	2.92	1.20
	(−)	72,148	1142	18.4	0.0068	1309	25.9	0.0096	39.8	0.0148	2.17	1.15
-7	(+)	133,531	1897	18.4	0.0068	2230	31.0	0.0115	46.5	0.0172	2.53	1.18
	(−)	122,041	1962	21.0	0.0078	2187	30.0	0.0111	45.5	0.0169	2.17	1.11

Fig. 14. Determination of yield strength.

Fig. 16. Curves of stiffness versus top displacement.
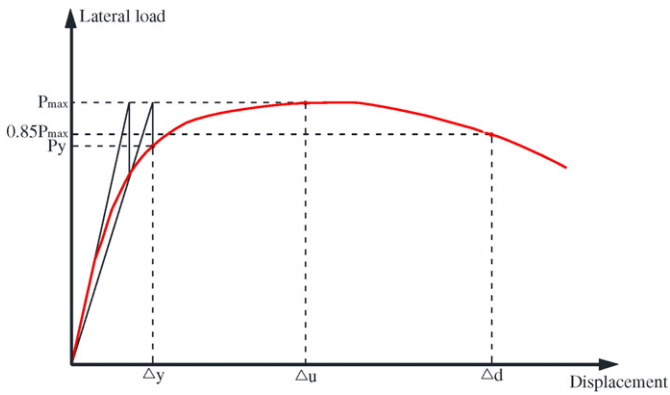
3. The cyclic stiffness of the specimens degrades steadily and almost linearly from the yielding point up to the failure point. It can be concluded that the stiffness deterioration is more noticeable after the specimen began to yield, and the steep drop in stiffness mainly results from the cumulative plastic deformation.

4. The initial stiffness is largely affected by the cross-sectional area. As shown in Fig. 16, the stiffness of Specimen -7 is obviously much higher than the other specimens due to the significantly larger cross section of 2600 mm × 1924 mm. The axial load ratio also has influence on the stiffness as mentioned in Section 4.1. Higher axial load ratio aggravates the energy absorption capacity and leads to the decrease in stiffness.

4.4. Ductility

Ductility is defined as the ability of the structure to undergo large plastic deformation without obvious loss of strength. It is an important factor in the earthquake-resistant design of structures. The assessment of ductility for specimens can be carried out by calculating ductility ratio, which is defined as the ratio of the ultimate displacement to the yielding one as given in Eq. (5). The ductility ratio represents the capacity of the specimen to develop nonlinear deformation without extensive damage. Table 3 lists the yield displacement (d_y), yield load (P_y), ultimate displacement (d_u), ultimate load (P_u) and ductility ratio (μ), where (+) denotes the upper semi-cycles and (−) denotes the lower semi-cycles.
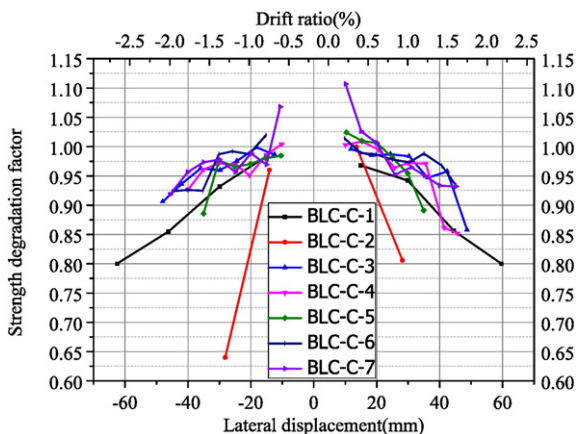
$$\mu = \frac{d_u}{d_y} \tag{5}$$

where d_y is the displacement corresponding to the yield strength and d_u is the displacement corresponding to the designed ultimate strength, which is defined as the post-peak displacement when the lateral force decreases to 85% of the peak load ($0.85F_{max}$). The conclusions can be drawn as follows:

1. As expected, the specimen exhibits good ductility. The ductility ratio of the connection ranges from 1.80 to 3.69. The specimens have satisfactory deformation capacity after the yielding of the specimens. The ratio of the peak load to the yield load ranges from 1.11 to 1.40, which indicates that a reasonable safety reserve has been maintained.

2. The yield displacements for Specimens -1 and -2 are similar, while the displacement at peak load and the ultimate displacement of Specimen -1 are larger than those of Specimen -2. The same observation can be found among the Specimens -3, -4 and -5. Therefore, an increase in axial force ratio has a minimal effect on the yield displacement and meanwhile, reduces the ultimate displacement and leads to a drop in the ductility ratio.

3. Both the yield and ultimate displacements for Specimen -7 are larger than Specimen -4, while the latter specimen has greater displacements than Specimen -2. It thus demonstrates that the extent of the cross-sectional area of the specimen has a significant impact on the deformation capacity of the wall.

4. Comparison among Specimens -2, -4 and -6 shows a relatively large ultimate displacement for Specimen -6, which means that the enhancement of the boundary element of the specimen and more compartments of the wall body divided by vertical webs improve the wall's deformation capacity.

5. The presence of welded shear studs increases the yield displacement for Specimen -5 when compared with Specimen -4. However, the unexpected out-of-plane deformation in Specimen -5 during the test restrains the development of deformation under cyclic loading, which finally results in a relatively small ultimate displacement and a poor ductility ratio for Specimen -5.

4.5. Energy dissipation capacity

The inelastic deformation of the connections aids the energy dissipation in an earthquake through hysteresis behavior, thereby reducing the transmitted energy to other structural elements. This can help to improve the seismic performance of the whole structural system subjected to strong earthquakes. As shown in Fig. 18, the energy absorbed by the deformation of the specimen can be measured as the areas enclosed by the force–displacement hysteresis loop. This is the total plastic work performed by the specimen. The equivalent damping coefficient h_e is
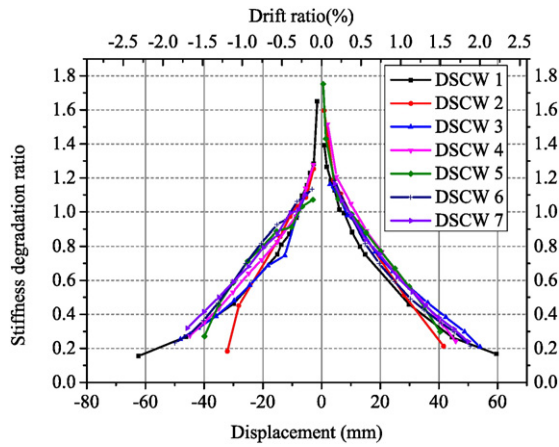

Fig. 15. Strength degradation of specimens.

Fig. 17. Stiffness degradation ratio versus top displacement response.

identified by Eq. (6). The results are presented in Table 4, and the h_e–θ curves of the specimens are shown in Fig. 19.

$$h_e = \frac{S_{(ABC+CDA)}}{2\pi S_{(OBE+ODF)}} \qquad (6)$$

where $S_{(ABC+CDA)} = $ area enclosed by the hysteresis loop and $S_{(OBE+ODF)} = $ summation of the triangle areas OBE and ODF.

As expected, the energy dissipation of the specimen, which can be identified as $S_{(ABC+CDA)}$, gradually increases by increasing the displacement amplitudes of the hysteresis loops up to the failure point. Specimen -2 exhibits the poorest energy dissipating capacity. Although the energy absorbed per cycle by Specimen -2 is similar to that by the other specimens, the least hysteresis cycles were observed in Specimen -2. Therefore, the cumulative energy dissipated by Specimen -2 is the lowest. The best cumulative energy dissipation capacity is found in Specimen -7. The deformation capacity of Specimens -6 and -7 is similar; the latter however, possesses greater strength than the former, which indicates that the latter has a larger cumulative energy dissipation capacity.

The axial force ratio has significant impact on the cumulative energy dissipation capacity. The cumulative dissipated energy of Specimen -1 was higher than that of Specimen -2. This can be attributed to the fact that the former has a better deformation capacity than the latter. The deformation capacity among Specimens -3 through -5 is similar, but Specimen -3 exhibits the best ability in absorbing energy because the energy dissipated per cycle by Specimen -3 is the largest.

The equivalent damping coefficient stably goes up with the increase in the displacement level. It stays at a low level of around 0.5 before the
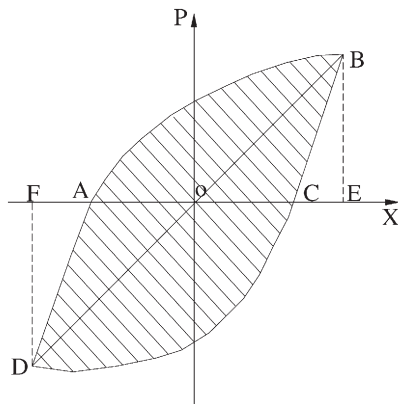
Table 4
Equivalent damping coefficient.

Specimen	Displacement	$S_{(ABC+CDA)}$	$S_{(OBE+ODF)}$	h_e
-1	$1\triangle_y$	8937	12,087	0.118
	$2\triangle_y$	35,561	29,692	0.191
	$3\triangle_y$	75,581	41,099	0.293
-2	$1\triangle_y$	5283	9777	0.086
	$2\triangle_y$	32,653	26,172	0.199
-3	$1\triangle_y$	5506	10,217	0.086
	$1.5\triangle_y$	10,795	19,675	0.087
	$2\triangle_y$	23,362	29,561	0.126
	$2.5\triangle_y$	37,320	38,216	0.155
	$3\triangle_y$	53,900	45,916	0.187
	$3.5\triangle_y$	71,620	51,868	0.220
-4	$1\triangle_y$	3366	7234	0.074
	$1.5\triangle_y$	7348	14,978	0.078
	$2\triangle_y$	15,231	23,698	0.102
	$2.5\triangle_y$	27,384	31,180	0.140
	$3\triangle_y$	39,819	41,920	0.151
	$3.5\triangle_y$	55,445	41,404	0.213
-5	$1\triangle_y$	2497	6760	0.059
	$1.5\triangle_y$	5253	14,394	0.058
	$2\triangle_y$	11,187	21,541	0.083
	$2.5\triangle_y$	21,238	30,101	0.112
	$3\triangle_y$	34,510	36,028	0.152
	$3.5\triangle_y$	52,877	39,930	0.211
-6	$1\triangle_y$	4511	9186	0.078
	$1.5\triangle_y$	7492	16,188	0.074
	$2\triangle_y$	16,769	25,622	0.104
	$2.5\triangle_y$	26,371	34,470	0.122
	$3\triangle_y$	46,304	41,027	0.180
	$3.5\triangle_y$	59,665	46,621	0.204
	$4\triangle_y$	78,499	50,126	0.249
	$4.5\triangle_y$	91,632	51,082	0.285
-7	$1\triangle_y$	6627	13,973	0.075
	$1.5\triangle_y$	11,296	24,942	0.072
	$2\triangle_y$	22,648	38,865	0.093
	$2.5\triangle_y$	43,562	56,028	0.124
	$3\triangle_y$	62,117	67,328	0.147
	$3.5\triangle_y$	86,916	77,446	0.179
	$4\triangle_y$	112,988	83,561	0.215

specimen yields. During the stage between the yielding of the wall and reaching the peak load, the equivalent damping coefficient increases and normally ranges from 0.15 to 0.20. The final equivalent damping coefficient is generally over 0.20 for most specimens, which means the specimens can offer sufficient energy dissipation capacity.

5. Summary and conclusions

In this paper, an innovative composite wall, named bundled lipped channel–concrete (BLC–C) composite wall was proposed. To investigate

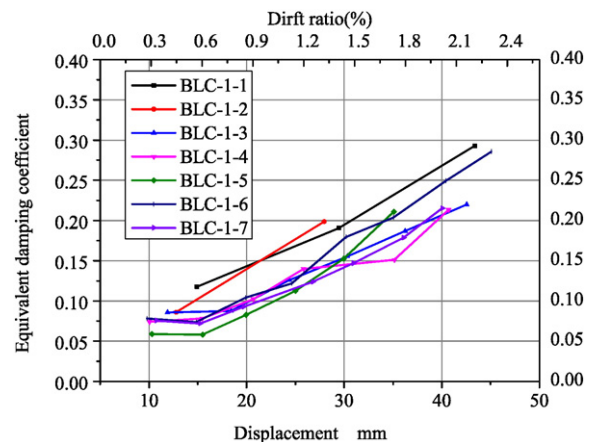Fig. 18. Equivalent damping coefficient calculation diagram.

Fig. 19. Energy dissipation.

the cyclic behavior of the specimens, seven full-scaled subassemblage tests were conducted under cyclic loading. Based on the test results, the following conclusions are made:

1) The specimens experienced similar damage patterns and failed in the sequence of local buckling of the steel sheets, and fracture development at the boundary of the wall. The lateral force versus top displacement curves showed stable and plentiful hysteresis behavior without pinching.

2) The reinforcement of the boundary element significantly affects the seismic performance of the composite walls. Enhancing the boundary element results in the reduction in the strength and stiffness deterioration and increases the deformation and energy dissipation capacity.

3) The impact of axial load ratio on the structural behavior of the walls is significant. An increase in the axial load ratio aggravates the hysteresis performance and accelerates the degradation of the strength and stiffness. However, the axial load ratio does not obviously affect the yield and peak strength of the specimens.

4) The presence of shear studs could prevent the steel sheets from local buckling and allows the steel and concrete to act compositely and thus, increased the yield strength and delayed the occurrence of fracture and failure. On the other hand, it shows a negligible effect on the entire hysteresis behavior, deformation capacity and energy dissipation.

5) For a wall with a certain length, more plentiful hysteresis loops could be reached by using lipped channels with a smaller cross-sectional area in the wall body, which results in more "webs" acting as transverse vertical stiffeners inside the specimen, which in turn, significantly enhances the specimens.

This paper focuses on the experimental investigation on the proposed walls. As future work (currently in progress), the authors are undertaking the task of finding design solutions.

Acknowledgements

References

[1] J.H. Thomsen, J.W. Wallace, Displacement-based design of slender reinforced concrete structural walls-experimental verification, J. Struct. Eng. 130 (4) (2004) 618–630.
[2] EN 1998-1, Eurocode 8: Design of Structures for Earthquake Resistance—Part 1: General Rules, Seismic Action and Rules for Buildings, European Committee for Standardization, CEN, Brussels, 2004.
[3] ACI 318-08, Building Code Requirements for Structural Concrete and Commentary, American Concrete Institute, Farmington Hills, 2008.
[4] NZS 3101-2006, Concrete Structure Standard, Standard New Zealand, Wellington, 2006.
[5] GB 50011-2010, Code for Seismic Design of Buildings, China Ministry of Construction, Beijing, 2010.
[6] Q. Zhao, A. Astaneh-Asl, Cyclic behavior of traditional and innovative composite shear walls, J. Struct. Eng. 130 (2) (2004) 271–284.
[7] J.W. Berman, Seismic behavior of code designed steel plate shear walls, Eng. Struct. 33 (2011) 230–244.
[8] J.G. Nie, L. Zhu, J.S. Fan, Y.L. Mo, Lateral resistance capacity of stiffened steel plate shear walls, Thin-Walled Struct. 67 (2013) 155–167.
[9] F. Vecchio, J. Frank, I. McQuade, Towards improved modeling of steel–concrete composite wall elements, Nucl. Eng. Des. 241 (8) (2011) 2629–2642.
[10] D. Dan, A. Fabian, V. Stoian, Theoretical and experimental study on composite steel–concrete shear walls with vertical steel encased profiles, J. Constr. Steel Res. 67 (5) (2011) 800–813.
[11] K.M.A. Hossain, H.D. Wright, Experimental and theoretical behaviour of composite walling under in-plane shear, J. Constr. Steel Res. 60 (2004) 59–83.
[12] T.S. Eom, H.G. Park, C.H. Lee, J.H. Kim, I.H. Chang, Behavior of double skin composite wall subjected to in-plane cyclic loading, J. Struct. Eng. 135 (10) (2009) 1239–1249.
[13] H.S. Hu, J.G. Nie, M.R. Eatherton, Deformation capacity of concrete-filled steel plate composite shear walls, J. Constr. Steel Res. 103 (2014) 148–158.
[14] J. Qian, Z. Jiang, X. Ji, Behavior of steel tube-reinforced concrete composite walls subjected to high axial force and cyclic loading, Eng. Struct. 36 (2012) 173–184.
[15] X. Ji, F. Jiang, J. Qian, Seismic behavior of steel tube–double steel plate–concrete composite walls: experimental tests, J. Constr. Steel Res. 86 (2013) 17–30.
[16] GB 50010-2010, Code for Design of Concrete Structures, China Ministry of Construction, Beijing, 2010.
[17] JGJ 101-96, Specification of Testing Methods for Earthquake Resistant Building. China Planning Press, Beijing, 1997.
[18] Y. Qin, Z. Chen, X. Wang, Experimental investigation of new internal-diaphragm connections to CFT columns under cyclic loading, J. Constr. Steel Res. 98 (2014) 35–44.
[19] J.G. Nie, H.S. Hu, J.S. Fan, et al., Experimental study on seismic behavior of high-strength concrete filled double-steel-plate composite walls, J. Constr. Steel Res. 88 (2013) 206–219.